nanomaterials

MDPI

Article

MOS Capacitance Measurements for PEALD TiO_2 Dielectric Films Grown under Different Conditions and the Impact of Al_2O_3 Partial-Monolayer Insertion

William Chiappim [1,2,*], Marcos Watanabe [2], Vanessa Dias [3], Giorgio Testoni [3], Ricardo Rangel [2], Mariana Fraga [4], Homero Maciel [3,5], Sebastião dos Santos Filho [2] and Rodrigo Pessoa [3,5,*]

1 i3N, Departamento de Física, Universidade de Aveiro, Campus Universitário de Santiago, 3810-193 Aveiro, Portugal
2 Laboratório de Sistemas Integráveis, Escola Politécnica da Universidade de São Paulo (USP-SP), 05508-010 São Paulo, Brazil; marcosnwatanabe@gmail.com (M.W.); rrangel@lsi.usp.br (R.R.); sgsantos@lsi.usp.br (S.d.S.F.)
3 Laboratório de Plasmas e Processos (LPP), Instituto Tecnológico de Aeronáutica (ITA), 12228-900 São José dos Campos, Brazil; van_ametista@yahoo.com.br (V.D.); giorgiotestoni@gmail.com (G.T.); homero@ita.br (H.M.)
4 Instituto de Ciência e Tecnologia, Universidade Federal de São Paulo, 12231-280 São José dos Campos, Brazil; mafraga@ieee.org
5 Instituto Científico e Tecnológico, Universidade Brasil, 08230-030 São Paulo, Brazil
* Correspondence: wcj@ua.pt (W.C.); rspessoa@ita.br (R.P.)

Received: 15 January 2020; Accepted: 13 February 2020; Published: 17 February 2020

Abstract: In this paper, we report the plasma-enhanced atomic layer deposition (PEALD) of TiO_2 and TiO_2/Al_2O_3 nanolaminate films on p-Si(100) to fabricate metal-oxide-semiconductor (MOS) capacitors. In the PEALD process, we used titanium tetraisopropoxide (TTIP) as a titanium precursor, trimethyl aluminum (TMA) as an aluminum precursor and O_2 plasma as an oxidant, keeping the process temperature at 250 °C. The effects of PEALD process parameters, such as RF power, substrate exposure mode (direct or remote plasma exposure) and Al_2O_3 partial-monolayer insertion (generating a nanolaminate structure) on the physical and chemical properties of the TiO_2 films were investigated by Rutherford backscattering spectroscopy (RBS), Raman spectroscopy, grazing incidence X-ray diffraction (GIXRD), and field emission scanning electron microscopy (FESEM) techniques. The MOS capacitor structures were fabricated by evaporation of Al gates through mechanical mask on PEALD TiO_2 thin film, followed by evaporation of an Al layer on the back side of the Si substrate. The capacitors were characterized by current density-voltage (J-V), capacitance-voltage (C-V) and conductance-voltage (G-V) measurements. Our results indicate that RF power and exposure mode promoted significant modifications on the characteristics of the PEALD TiO_2 films, while the insertion of Al_2O_3 partial monolayers allows the synthesis of TiO_2/Al_2O_3 nanolaminate with well-spaced crystalline TiO_2 grains in an amorphous structure. The electrical characterization of the MOS structures evidenced a significant leakage current in the accumulation region in the PEALD TiO_2 films, which could be reduced by the addition of partial-monolayers of Al_2O_3 in the bulk of TiO_2 films or by reducing RF power.

Keywords: plasma-enhanced atomic layer deposition; titanium dioxide; nanolaminate; metal-oxide-semiconductor; electrical properties

1. Introduction

Titanium dioxide (TiO_2) thin films and nanolaminates have a significant number of promising applications in different areas, such as microelectronics [1–6], photovoltaics [7,8], photocatalysis [9–11],

fuel cells [12], sensors [13–16], anti-reflective coating applications [17], biomedical coatings [18,19] and food packaging applications [20]. The properties and applicability of TiO_2 thin films are intrinsically related to their crystal structure. In this sense, they have been mainly produced in amorphous, anatase and/or rutile structure forms by a wide range of techniques, namely sol-gel [21,22], magnetron sputtering [23,24], chemical vapor deposition (CVD) [25], physical vapor deposition (PVD) [26], atomic layer deposition (ALD) [27,28] and plasma-enhanced atomic layer deposition (PEALD) [29–34]. Among them, PEALD requires lower substrate and process temperatures to obtain crystalline films [35]. It is also one of the most promising technologies for the growth of conformal coatings and nanolaminates in various structures and topographies [32,36] with layer thickness precisely defined by self-limited surface reactions [37]. During the PEALD of metal oxide films, oxygen (O_2) plasma is used as an oxidant source [38]. The plasma is composed of a mixture of electrons, ions, neutrals and excited molecules/atoms. The action of each specie depends on the plasma exposure mode that can be remote or direct, where the latter allows contact of all plasma species with surface ligand groups [39]. The oxidizing plasma source used in the PEALD process has the advantage of reducing the purge time after the precursor pulse. Furthermore, its high reactivity enhances surface chemical reactions, allowing the process to be carried out at lower temperature and, consequently, preventing the interlayer diffusion that is responsible for the degradation of nanoscale device properties [40].

Because of its dielectric properties, TiO_2 thin films are widely used in microelectronic and photovoltaic applications. In microelectronic devices and systems, the metal oxide deposition temperatures need to be below 500 °C because capacitors are expected to be deposited after the formation of transistors [41]. The same caution is required for the insulator/oxide deposition temperature in photovoltaic cells since temperatures above 300 °C cause degradation in these devices related to one order vacancy compound (OVC) [42]. The PEALD technique fits the requirements for both aforementioned devices, as it offers excellent uniformity, conformability and atomic level control of the growing oxide layer [43]. Moreover, as previously stressed, TiO_2 growth can be conducted at lower process temperatures and under atmospheres with shorter purge pulses in PEALD reactors than in standard thermal ALD [44].

In our previous study [45], the effects of O_2 plasma power, titanium precursor chemistry and plasma exposure mode on the growth mechanism, structure and morphology of PEALD TiO_2 films were investigated. Herein, we extend this study with the focus on the fabrication and characterization of TiO_2/p-Si MOS capacitors for potential applications in microelectronic and photovoltaic devices. J-V, C-V and G-V characteristics of the MOS capacitors at room temperature were investigated in function of the following PEALD process parameters: (i) RF power, (ii) plasma exposure mode and (iii) Al_2O_3 partial monolayer insertion (generating a nanolaminate structure). In addition, we also discuss how the plasma exposure affects or causes surface modifications and changes in electrical parameters of TiO_2 films. There is a lack of available literature on the electrical characteristics of MOS capacitors formed by PEALD TiO_2-based films on p-type Si substrates grown under different conditions.

2. Materials and Methods

2.1. Film Preparation

PEALD processes were performed in a Beneq TFS 200 ALD system (Beneq Oy, Espoo, Finland) equipped with a capacitively coupled plasma reactor, as illustrated in the schematic diagram shown in Figure 1. The reactor consists of a cylindrical chamber, with a 200 mm diameter, composed by two zones: (i) the upper plasma generation zone, where the plasma is generated by capacitive coupling of the upper plate with a 13.56 MHz RF power supply (Cesar, Advanced Energy Inc., Fort Collins, CO, USA) and grounding the bottom grid electrode plus radial reactor walls; and (ii) the lower process zone (sample stage), where there is no plasma generation. As the plasma generation zone is located at a distance from the process zone, the ion damage should be significantly suppressed [46]. In our experiments, the spacing between the top plate and the grid was 30 mm, whereas between the grid and

the substrate holder, it was 12 mm (Figure 1a). In the second plasma exposure configuration shown in Figure 1b, we removed the grid, and the sample was exposed to the plasma generation zone. Thus, the damage caused by the ion impact on the substrate surface must be higher [46]. These PEALD reactor configurations schematized in Figure 1a,b are named remote plasma mode and direct plasma mode, respectively [38].

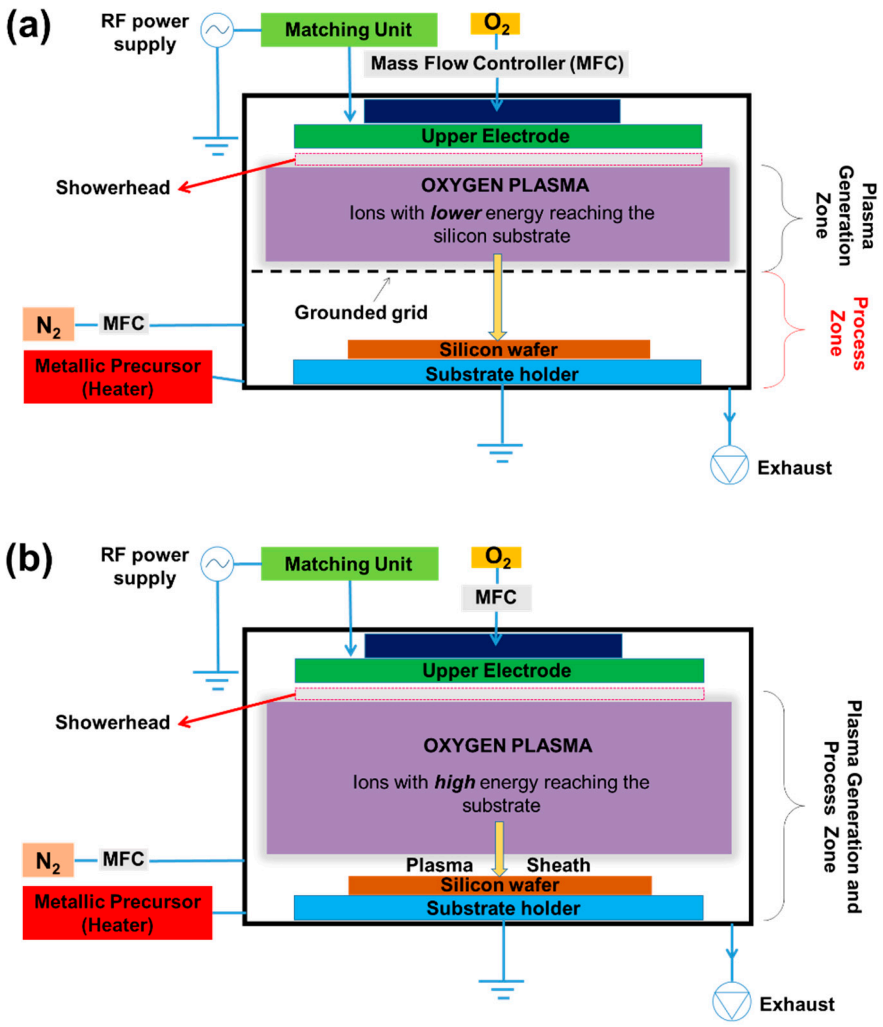

Figure 1. Schematic diagram of the capacitively coupled plasma reactor used for plasma-enhanced atomic layer deposition (PEALD) processes: (**a**) remote plasma mode and (**b**) direct plasma mode.

The substrates used for TiO_2 thin-film deposition were three-inch p-type <100> silicon wafers (UniversityWafer Inc., South Boston, MA, USA) chemically cleaned, using a modified RCA recipe described in [47]. Between each bath, the Si wafers were washed in deionized (DI) water for 5 min. Subsequently, they were dipped in diluted hydrofluoridric acid, in the proportion 80:1 (80 H_2O + 1 HF (49%)), at room temperature, for 100 s, and were rinsed in DI water for 3 min.

TiO_2 thin films were grown using titanium (IV) isopropoxide (TTIP, 97.0%, Sigma-Aldrich, São Paulo, Brazil) as a metallic precursor and O_2 gas (99.99%, White Martins, Jacareí, Brazil) to generate the O_2 plasma (oxidant precursor). Here, the TTIP precursor was heated at 70 °C to obtain a high vapor pressure, and nitrogen (99.999%, White Martins, Jacareí, Brazil) was used as the gas of purge. The vapor delivery line of the TTIP was also heated to 70 °C, to prevent precursor condensation. The insertion of the oxygen gas was through the upper plate of the plasma generation zone at a flow rate of 50 sccm. Before the deposition process, the reactor chamber was evacuated at a pressure of 10^{-2} mbar, and the N_2 gas purge was maintained around 1.0 mbar through the insertion of 250 sccm. The

reactor temperature was fixed at 250 °C for all processes, and its variation during the film growth did not exceed 3 °C. For PEALD TiO_2 processes, the reaction cycle number was maintained at 1000. The self-bias voltage varied by approximately 70–100 V during the 100–150 W O_2 plasma pulse. This voltage drop value in the plasma sheath (see Figure 1b) is sufficient to supply energy to the ions, to induce chemical reactions in growing film during PEALD [48].

The experimental procedure for the deposition of TiO_2 thin films was divided into three sets of experiments. In the first set, the RF power was varied between 100 to 150 W. Concomitantly, in the second set the plasma exposure mode was varied to study the impact of direct plasma exposition during the ligand pulse. In the third set, Al_2O_3 partial-monolayers were grown with TiO_2 by alternating cycles of TiO_2 and Al_2O_3 in supercycles, in order to form a TiO_2/Al_2O_3 nanolaminate. For this latter, the experimental parameters are detailed in the next subsection.

2.2. Nanolaminate Preparation

TiO_2/Al_2O_3 nanolaminate structure was prepared, using the design proposed by Testoni et al. [49], i.e., alternatively depositing a TiO_2 sublayer and Al_2O_3 partial-monolayer, respectively, in "*n*" supercycles. The Al_2O_3 is formed by a single cycle of trimethylaluminum (TMA)–O_2 plasma, so it is a partial-monolayer because of steric hindrance of the precursors, while the TiO_2 sublayer is formed by repeating 60 cycles of TTIP–O_2 plasma. This condition is in the interface of the TiO_2 crystallization disruption [49]. Here, the Al_2O_3 partial-monolayers were grown, using TMA (97%, Sigma-Aldrich, São Paulo, Brazil) at 21 °C and O_2 plasma. TiO_2 sublayers were deposited, using TTIP at 70 °C and O_2 plasma. High purity N_2 was used as purge and carrier gas for both TMA and TTIP precursors. The base pressure of the reactor was below 10^{-2} mbar, and, during the deposition, the gas pressure was maintained around 1.0 mbar through the insertion of 300 sccm of nitrogen. The TiO_2/Al_2O_3 films were grown under the following conditions of supercycle: 1 cycle of TMA–O_2 plasma per 60 cycles of TTIP–O_2 plasma. The supercycle was repeated until 2700 cycles of TTIP–O_2 plasma, resulting in 45 layers of TiO_2/Al_2O_3. The temperature and RF power were fixed at 250 °C and 100 W, respectively, and the PEALD reactor was operated in remote mode.

2.3. Thin-Film Characterization

Rutherford backscattering spectroscopy (RBS) was used to determine the film thickness and film elemental composition (in at. %). The measurements were performed in a Pelletron-type accelerator, using a 2.2 MeV $4He^+$ beam, and the particle detector was positioned at an angle of 170° to the incident beam. The detection sensibility of RBS in relation to Ti, O, Al and Si is approximately 5%. The RBS data were analyzed, using the computer code MultiSIMNRA [50,51]. The theoretical density considering the TiO_2 crystal structure was applied to convert the RBS density values (10^{15} atoms.cm^{-2}) into the thickness (nm) of the layer. Raman scattering measurements were used for microstructural analysis of the samples. The Raman spectra were recorded at room temperature, with a Raman microspectrometer (Horiba, Evolution, Kyoto, Japan) equipped with a thermoelectrically cooled multichannel charge-coupled device detector. The spectral resolution was better than 1 cm^{-1} over the range from 100 to 900 cm^{-1}, and the power of the incident laser beam on the samples was <10 mW, with an excitation wavelength of 532 nm. Phonons modes were then analyzed by fitting Raman peaks with a Voigt profile, fixing the Gaussian linewidth (1.6 cm^{-1}) to the experimental setup resolution. In order to characterize the crystalline structure, the grazing incidence X-ray diffraction (GIXRD) method was used. GIXRD patterns were obtained at room temperature, in a Shimadzu XRD 6000 goniometer, using cooper target (CuK_α radiation 1.5418Å), 2θ from 20° to 80°, at a scanning speed of 0.02°/s, a voltage of 40 kV and a current of 30 mA. Moreover, the GIXRD studies were carried out at an incidence angle of 0.29°. The morphology of the samples was evaluated in a Tescan Mira (TESCAN Brno, s.r.o., Kohoutovice, Czech Republic) field emission scanning electronic microscopy (FESEM), coupled with an AZtec 3.1 energy-dispersive X-ray spectrometer (EDS).

2.4. Fabrication and Characterization of the MOS Structures

Aluminum (Al) was evaporated on the PEALD TiO_2 films through a mechanical mask, to form Al gates with area of 4.3×10^{-3} cm^2 and thickness of approximately 200 nm. Subsequently, aluminum layers with a thickness of approximately 200 nm were evaporated on the backside of Si substrate. Thus, the MOS structure of the PEALD TiO_2/p-Si capacitors were formed. This fabrication process is illustrated in Figure 2.

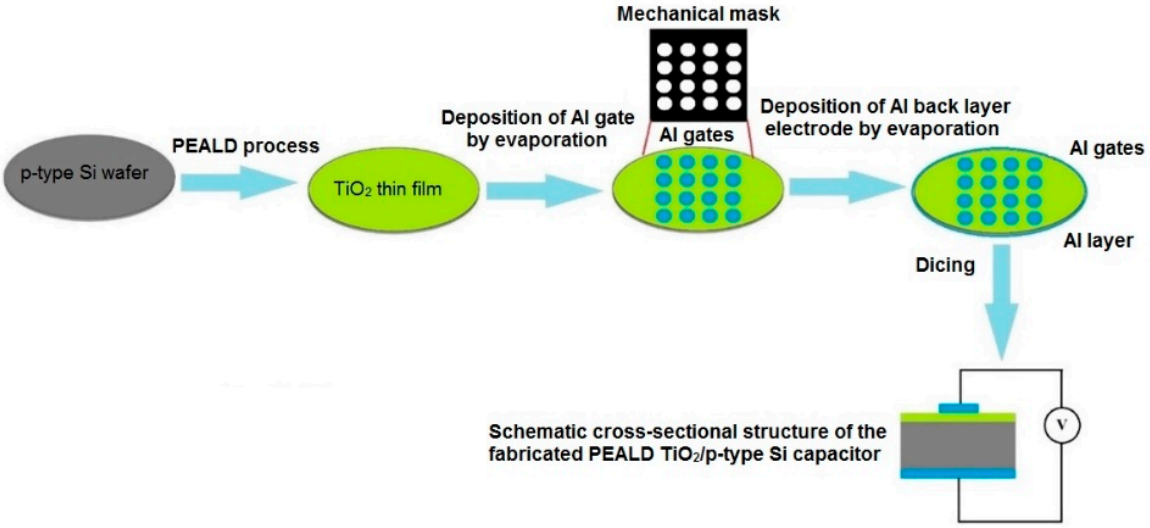

Figure 2. Schematic representation of the fabrication process of the PEALD TiO_2/p-type Si capacitors.

The dark current density-voltage (J-V) characteristics of the PEALD TiO_2/p-Si capacitors were measured at room temperature by an Agilent 4146 C source measurement unit (Keysight Technologies, São Paulo, Brazil) programmed to apply potentials on the metal gate between −10 V and +10 V in steps of 0.1 V/s. The capacitance-voltage (C-V) and conductance-voltage (G-V) characteristics of the capacitors were evaluated at 1 MHz and at room temperature, using an HP 4280A C meter/C-V plotter (Hewlett-Packard Inc., Palo Alto, CA, USA). Both types of equipment mentioned above are highly accurate with a low noise ground unit.

3. Results and Discussion

3.1. Film Characterization

3.1.1. Chemical Composition

Studies of stoichiometry throughout the TiO_2 and TiO_2/Al_2O_3 films' thickness were done, using RBS. Figure 3 shows the experimental and simulated RBS spectra for TiO_2 films deposited under different conditions of RF power, plasma mode and Al_2O_3 partial-monolayer insertion.

The backscattered signal from the TiO_2 film on the Si substrate is characterized by well-defined peaks of Ti and O. These peaks depend on the backscattering cross-section, and the areas below the peaks represent the areal density of the atom. Most of the time, the peak position is not matched with the exact energy position of the atom. The Si substrate in the spectra is correlated with the pattern similar to a shoulder. Note that, in the case of TiO_2/Al_2O_3 nanolaminate, the Al peak is not evident; however, it is necessary to consider 9% of its elemental composition during the simulation of the experimental RBS spectrum, as shown in Figure 3e. This behavior occurs because (a) Si and Al have very close atomic numbers that cause an overlapping of their respective peaks, and (b) the amount of Al in the film is low due to the nature of the nanolaminate PEALD process that used a single cycle of TMA-O_2 plasma, while repeating 60 cycles of TTIP-O_2 plasma during each super-cycle. This results

in a low amount of Al in the film (9%), along with the reduced peak intensity in the RBS spectrum. The plasma mode, under the same RF power, does not significantly influence the film thickness. On the other hand, if the RF power is increased, the film thickness is reduced for both plasma modes. This behavior for the TTIP precursor was demonstrated in our previous study [45], where it was observed that the growth per cycle (GPC) decreases when RF power is increased. The leading cause is related to the increase of the density of O_2 radicals that fragments the TTIP-ligands, hindering the formation of Ti-O bonds due decreasing of the free path.

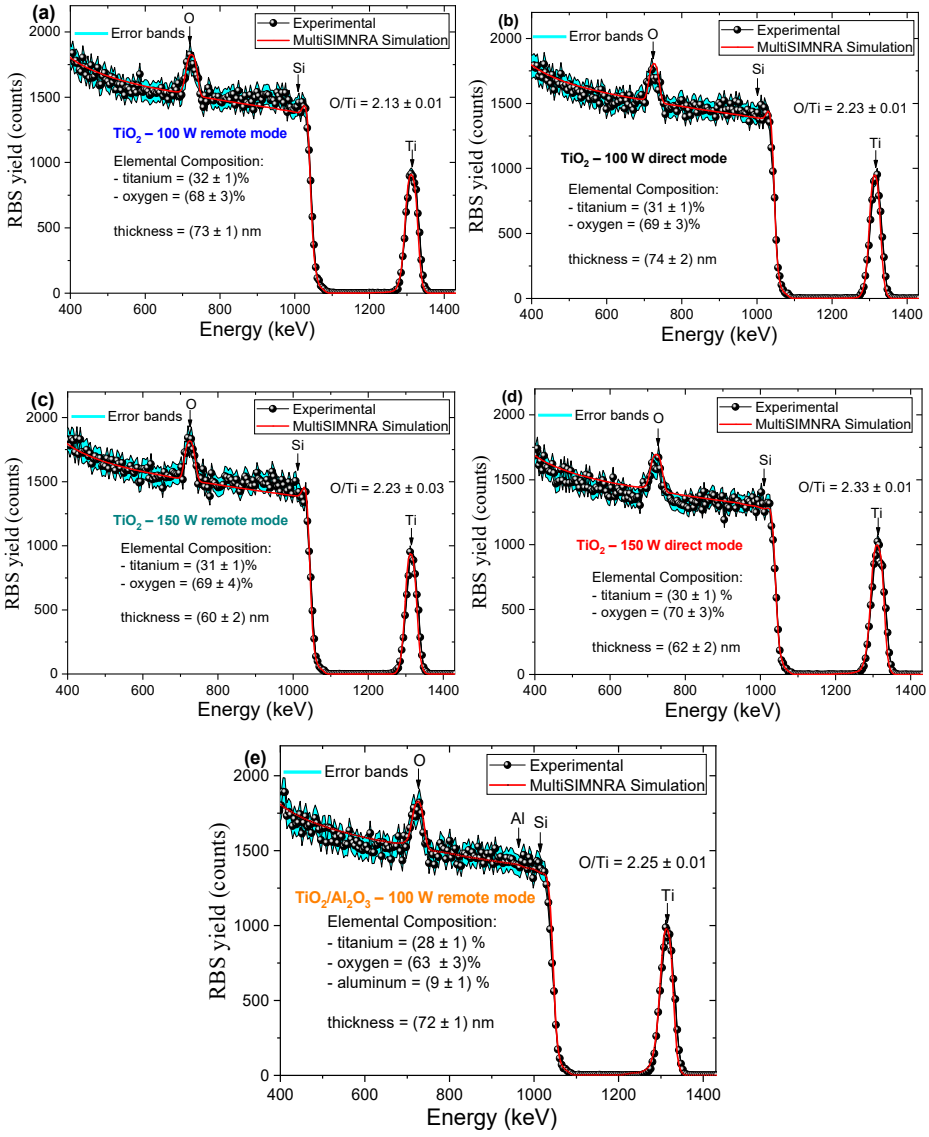

Figure 3. Experimental, simulated RBS spectra and data error bands for PEALD TiO_2 films deposited under different conditions: (**a**) 100 W in remote mode, (**b**) 100 W in direct mode, (**c**) 150 W in remote mode, (**d**) 150 W in direct mode and (**e**) 100 W in remote mode (TiO_2/Al_2O_3 nanolaminate). The precision was fixed in the MultiSIMNRA, at 10^{-7}, with the error bars in the simulated RBS spectra being smaller than the line size.

The insertion of Al_2O_3 partial-monolayers in TiO_2 using the nanolaminate design proposed by Testoni et al. [49] showed that a considerable increase of number of cycles (2700 cycles) was necessary for obtaining a film thickness near to pure TiO_2 condition (1000 cycles). This is due to the poisoning effect promoted by the TMA pulse, affecting the growth kinetics of subsequent TiO_2 layers, and thereby altering the overall growth per cycle (GPC) of TiO_2/Al_2O_3 nanolaminate [49].

The elemental chemical composition of the samples is shown, together with the RBS spectra, in Figure 3. The TiO_x films show an excess of oxygen, i.e., x values ranging from 2.13 ± 0.01 to 2.33 ± 0.01, as can be seen in Figure 3. These results differ from those described for thermal ALD TiO_2 films, in which either stoichometric or oxygen-deficient films are obtained [52]. The increase of oxygen content in PEALD TiO_2 films may be related to the higher reactivity of O_2 plasma compared to the water precursor used in thermal ALD. In a recent study, Wei et al. [5] showed the influence of temperatures on the PEALD process applied to the growth of TiO_2 films in Si for the manufacture of MOS capacitors, where they used O_2 plasma at 400 W of RF power. They varied the temperature from 100 to 300 °C, with steps of 50 °C. Using the X-ray photoelectron spectroscopy (XPS) technique, they verified that the TiO_2 films had O/Ti stoichiometry ranging from 2.08 to 2.32. These results are in agreement with our O/Ti stoichiometry RBS data. Raztsch et al. [35] found a slight increase in the oxygen content in TiO_2 films grown on Si by PEALD with O_2 plasma at 300 W. These TiO_2 films consist of large crystallites embedded in the amorphous layer, and, through RBS, they determined the O/Ti stoichiometry of 2.00 ± 0.04. Moreover, Bousoulas et al. verified that by increasing the oxygen content in TiO_2 films, the size of vacancy-based filaments is reduced, resulting in the more stable operation of resistive switching memory devices [53]. This can be an interesting application for the materials and devices reported in this study, especially for conditions of 100 W RF power and with the insertion of Al_2O_3. A more detailed explanation of the excess oxygen in the films is given in Section 3.1.2.

3.1.2. Structure and Morphology

Micro-Raman spectra are shown in Figure 4a. Four Raman-active modes associated with anatase structure can be observed: A_{1g} (519 cm^{-1}), B_{1g} (397 cm^{-1}) and E_g (144 and 636 cm^{-1}) with a strong peak at 144 cm^{-1} [28,54]. The crystalline condition of pure TiO_2 thin films due to the strong peak at 144 cm^{-1} is clearly evidenced. On the other hand, for the TiO_2/Al_2O_3 nanolaminate, the main peaks of the anatase phase were not observed, and the rutile phase is formed above 500 °C for silicon substrate [28,37,52,53], which suggests that the film is amorphous or partially crystalline. Figure 4b shows the micro-Raman spectra evidencing the shift and the full width at half maximum (FWHM) of the E_g peak at 144 cm^{-1}. According to Parker et al. [55] and Bassi et al. [56], the shift of the E_g peak and bandwidth are related to non-stoichiometry, while the latter also influences the crystal size of anatase TiO_2. Ratzsch et al. showed a slight excess in oxygen (O/Ti > 2) in high-density TiO_2 with large crystallites embedded in the amorphous layer [35]. They observed the same behavior for the E_g peak at 144 cm^{-1}, i.e., a shift and a broadband. Thus, the shift in the E_g peak and the bandwidth observed in Figure 4b for all PEALD TiO_2 films can be attributed to the increase in the oxygen content, corroborating with RBS results. It is noteworthy that all characterizations of the thin films were performed in different positions of the samples. Therefore, the oxygen excess is not localized.

To confirm the Raman results, GIXRD measurements were performed, using the same 0.29° incident angle for all films. This angle was used to reduce the reflections from the Si substrate [45]. Based on the powder diffraction file (JCPDS: 21–1272) [57], all diffraction peaks are identified for the TiO_2 films studied here, as shown in Figure 5.

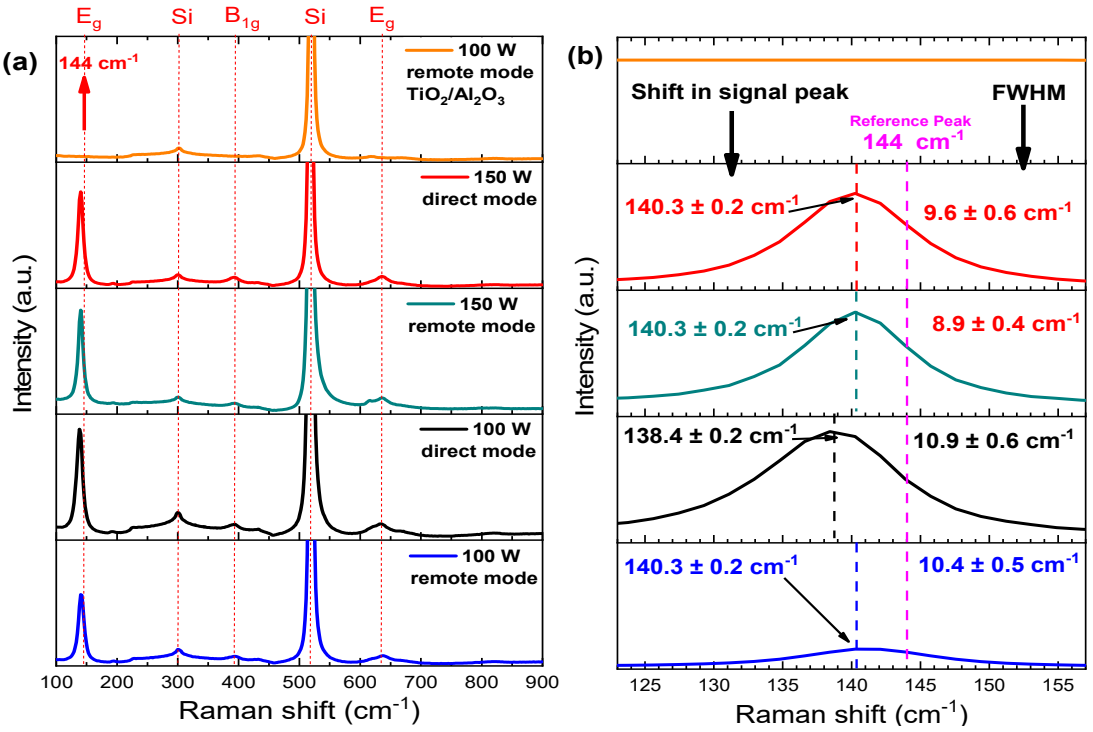

Figure 4. (**a**) Micro-Raman spectra for TiO_2 films deposited under different conditions of RF power, plasma mode and Al_2O_3 partial-monolayer insertion and (**b**) micro-Raman spectra evidencing the shift and the FWHM of the E_g peak at 144 cm^{-1}.

The grain size was calculated by using the Scherrer equation [59]; all the peaks of the anatase phase were considered in the calculations (Figure 5), with the values in the following order: (17.8 ± 0.7) nm to 150 W—direct mode, (19.2 ± 0.9) nm to 150 W—remote mode, (15.9 ± 0.8) nm to 100 W—direct mode and (16.2 ± 0.7) nm. These crystal sizes influence the broadband in Raman peaks [56]; however, when comparing the grain size found in the GIXRD diffractograms with the FWHM of the E_g peak found by the Raman spectrum, it is observed that the larger the grain size is, the smaller the FWHM is. Therefore, the film grown in 150 W—remote mode has the largest grain size with the smallest FWHM. On the other hand, the film grown with 100 W—direct mode has the largest FWHM and the smallest grain size. The results are in agreement with Parker et al. [55] and Bassi et al. [56]. Bearing in mind that there is no E_g peak for the TiO_2/Al_2O_3 film, and the error associated with the grain size is higher than the grain value, we could not find these parameters for this film.

Figure 6 shows FESEM images of the surface of the TiO_2 films grown at different PEALD process conditions. These images show that the grain size slight decreases with RF power for both plasma modes. The effect of the electrode grid was evidenced by the reduction of the action of the plasma ions during the capacitively coupled PEALD process [45]. As can be seen for both power values investigated, the change from remote to direct mode caused a slight reduction in grain size, probably due to the higher action of the species from plasma impinging on the substrate. An interesting result is presented in Figure 6e, where the insertion of Al_2O_3 partial-monolayers into TiO_2 film disrupts the growth of crystalline grains, creating only a few nanocrystalline grains in amorphous matrix [49].

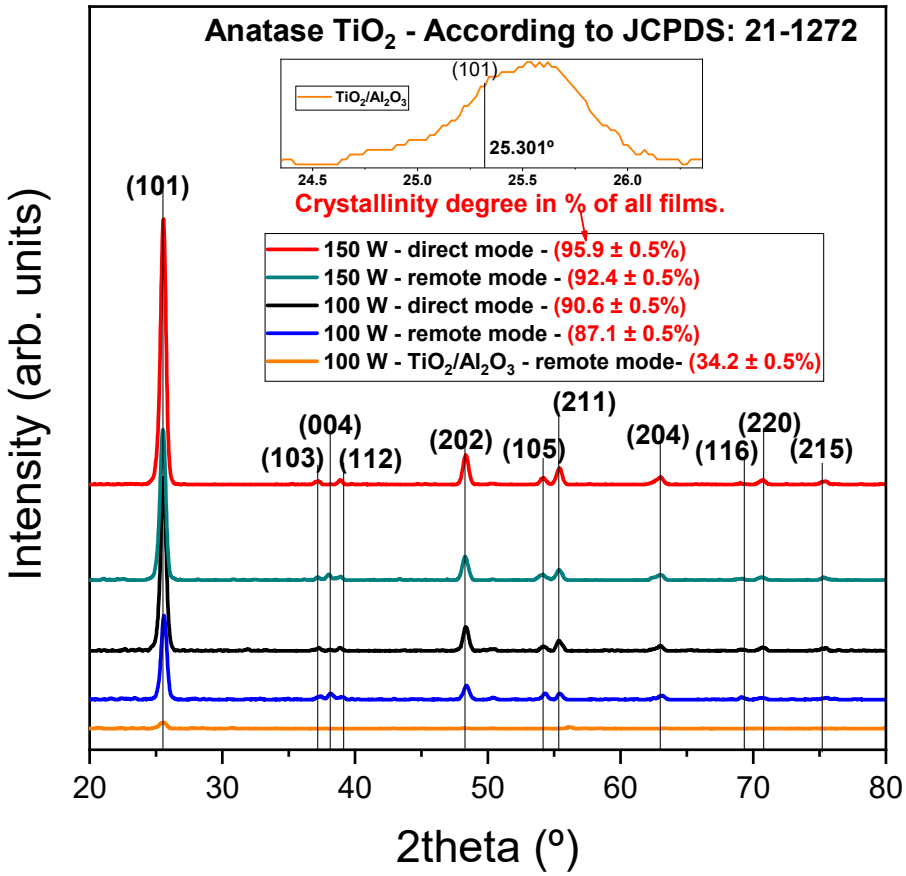

Figure 5. GIXRD diffractogram for TiO_2 films deposited under different conditions of RF power, plasma mode, and Al_2O_3 partial-monolayer insertion. Indexed peaks are of the anatase phase. The inset figure shows the peak (101) for the 100 W—TiO_2/Al_2O_3 film.

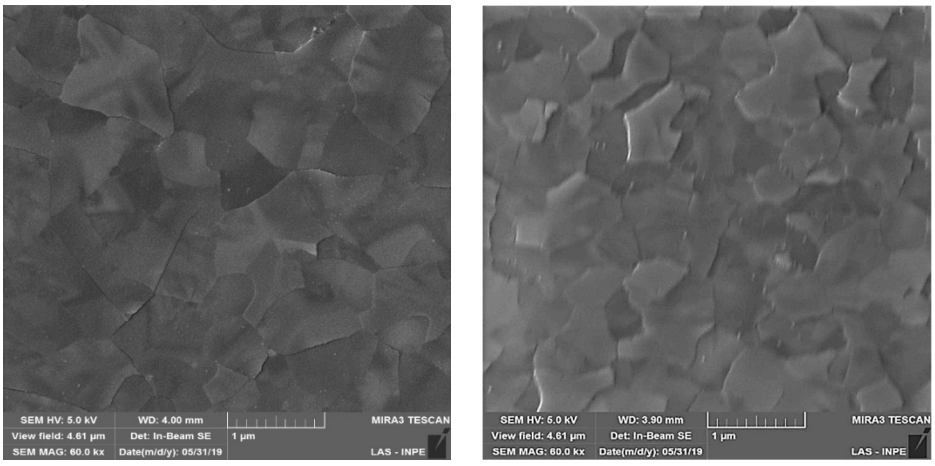

(**a**) (**b**)

Figure 6. *Cont.*

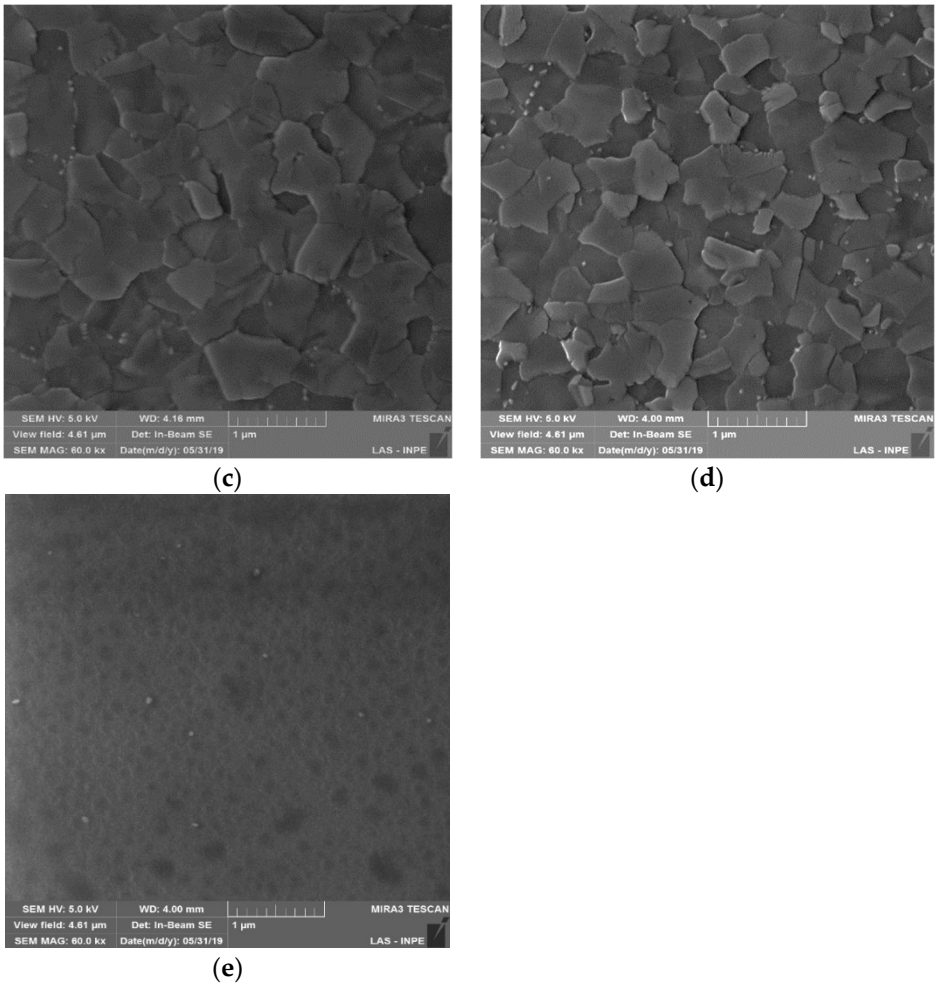

Figure 6. FESEM images of TiO_2 films deposited under RF power of (**a**) 100 W in remote mode, (**b**) 100 W in direct mode, (**c**) 150 W in remote mode, (**d**) 150 W in direct mode and (**e**) 100 W in remote mode (TiO_2/Al_2O_3 nanolaminate).

3.2. Electrical Characterization of TiO_2/p-Si MOS Capacitors

3.2.1. Current Density-Voltage Measurements

Electrical characterization was performed on the five PEALD TiO_2/p-type Si MOS structures fabricated at different values of RF power, substrate exposure mode and Al_2O_3 partial-monolayer insertion. Two sets of MOS current density were analyzed and presented in Figure 7: (i) one for TiO_2 samples with RF powers at 100 W and 150 W for remote and direct plasma modes (Figure 7a), and (ii) another for TiO_2/Al_2O_3 nanolaminate (Figure 7b). Figure 7d shows the dark J-V curve in semi-logarithmic scale under positive and negative biases at room temperature. As can be seen, the leakage current density at −2 V is in the order of 10^{-5}~10^{-4} A/cm^2, which is in the same order of magnitude reported by Wei et al. [5] and Baek et al. [1] that used PEALD and tetrakis dimethylamino titanium (TDMAT) as precursor to growth TiO_2 (20 nm) on Si.

To study the diode ideality factor (n), we used the dark J-V-adapted Ortiz-Conde model [60], which considers the equivalent circuit model, consisting of a single exponential type ideal junction, a series parasitic resistance (R_s) and a parallel parasitic conductance (G_p), as shown in Figure 7c. The $J(V)$ function of the equivalent circuit model is given by the following equation:

$$J = J_0\left(\exp\left(\frac{V - JR_s}{nV_{th}}\right) - 1\right) + (V - JR_s)G_p \quad (1)$$

where J is the current density, V is the terminal voltage, J_0 is the reverse saturation current density and $V_{th} = \frac{kT}{q}$ is the thermal voltage.

This implicit transcendental function cannot be explicitly resolved by using a standard elementary function. The solution depends on a particular function known as the *Lambert W* function [61]. By definition, this function is defined as the solution of the *Lambert W (x) exp (Lambert W(x)) = x*, where the solutions for each variable, J and V, are an explicit function of the other. Using the auxiliary Equation (1), we obtain the parameters a, b, c and d as a function of the equivalent circuit model:

$$a = \frac{1 + R_s G_p}{J_0} \tag{2}$$

$$b = \frac{J_0 - V.G_p}{J_0}, \tag{3}$$

$$c = \frac{-R_s}{nV_{th}}, \tag{4}$$

$$d = \frac{V}{nV_{th}}, \tag{5}$$

The general solution is as follows:

$$J = \frac{nV_{th}}{R_s} LambertW\left(\frac{J_0 R_s}{nV_{th}\left(1 + R_s G_p\right)} \exp\left(\frac{V + J_0 R_s}{nV_{th}\left(1 + R_s G_p\right)}\right)\right) + \frac{VG_p - J_0}{\left(1 + R_s G_p\right)} \tag{6}$$

This explicit analytic expression can be used to extract model parameters (Table 1) directly from the fit of experimental data, as shown in Figure 7c.

Table 1. Series parasitic resistance (R_s), parallel parasitic conductance (G_p) and the ideality factor calculated by the adjusting the J-V curves by the Ortiz-Conde model.

Sample	R_s (Ω)	G_p (μS)	n (Ideality Factor)
TiO_2-100 W remote mode	70	36	1.79
TiO_2/Al_2O_3-100 W remote mode	1110	6.8	1.59
TiO_2-100 W direct mode	180	256	1.93
TiO_2-150 W direct mode	47	89	1.99
TiO_2-150 W remote mode	50	84	1.99

Table 1 presents the diode ideality factor for all dark J-V curves fitted by Equation (6). As can be seen in Table 1, the ideality factor values occur between 1 and 2. Second, in the Shockley diffusion theory, which is based on the minority carrier diffusion predicted, n should be equal to 1 (next to an ideal junction) [62]. Sah et al. analyzed the generation and recombination in the space charge layer and predicted that $n \leq 2$ [63]. Faulkner and Buckingham [64] proposed a theory based in traps situated in depletion layer where the values of diode ideality factor occur between 1 and 2, which was experimentally verified by Nussbaum [65]. According to the aforementioned theories, the Ortiz-Conde model adjusted the experimental curves with good precision.

For 100 W RF power, ideality factor values decreased when the exposure mode changed from direct to remote. As the physical, chemical and morphological properties of the TiO_2 films synthesized in direct or remote mode are close, it is believed that the variation of n occurred because of changes in the sample's electrical properties, as reported in Table 1. Indeed, the mode change, as well as the RF power change, modified the R_s and G_p values of the films, where for 100 W RF power/direct mode, the series parasitic resistance achieved 180 Ω. On the other hand, for TiO_2/Al_2O_3 nanolaminate, the ideality factor was of 1.59, which suggests that the insertion of Al_2O_3 partial-monolayers can be used to adjust the n parameter. According to Jain and Kappor [66] and Shockley [62], n closer to 1 is more

efficient for DRAM capacitors and solar cell devices. In addition, Table 1 shows that this sample has a higher series parasitic resistance of 1100 Ω.

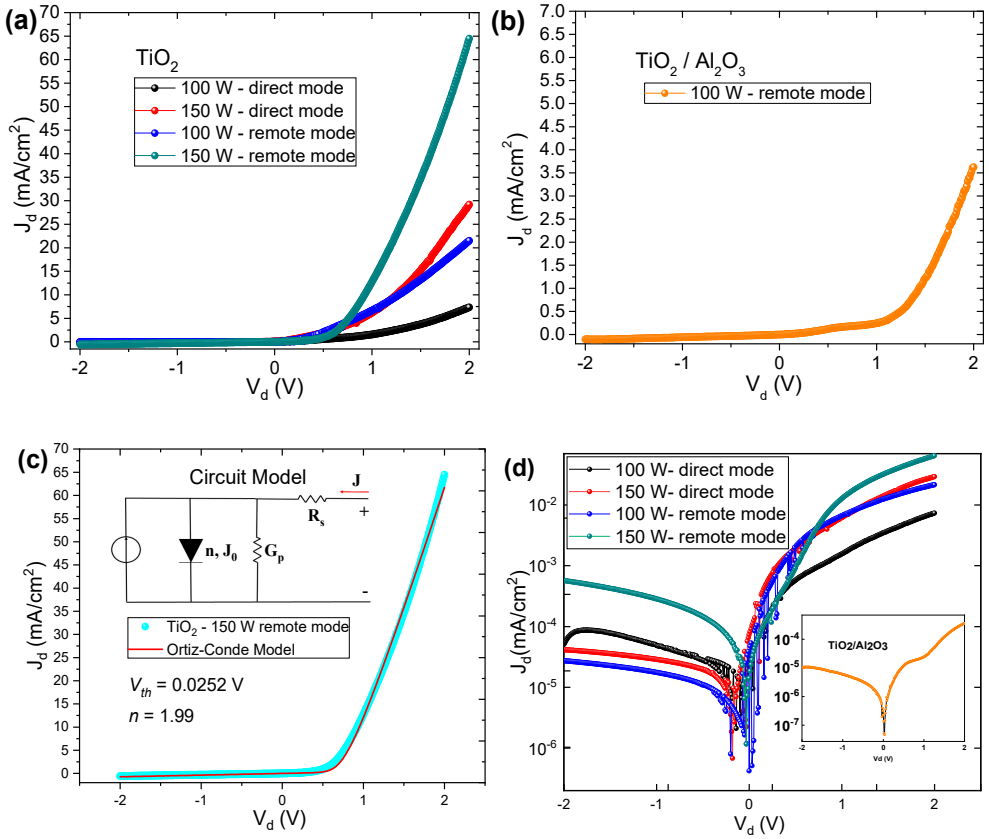

Figure 7. Dark J-V curves for the fabricated MOS capacitors: (**a**) TiO_2 films grown in remote and direct mode at 100 W and 150 W, (**b**) TiO_2/Al_2O_3 nanolaminate growth at 100 W, (**c**) adjustment of the curve (TiO_2-150 W/remote mode) through Ortiz-Conde model [60] and (**d**) dark J-V curves in semi-logarithmic scale, to show the leakage current density. The value of 0.995 was used for the determination coefficient (R-squared) to fit the J-V curve, using the Ortiz-Conde model. That is, 99.5% of the dependent variable was considered, with the error bars in the simulated J-V curves being smaller than the line size.

3.2.2. Capacitance-Voltage and Conductance-Voltage Measurements

C-V and G-V measurements were also performed to evaluate the electrical characteristics of the fabricated MOS capacitors. All the samples have presented a leakage current process through the TiO_2 layer.

Figure 8 shows the C-V and G-V curves for samples deposited in remote mode. The C-V curves showed a deep depletion region for all investigated cases, indicating the absence of an inversion layer due to the high leakage current through the TiO_2 films. By comparing the behavior of the C-V curve with the G-V curve for TiO_2 grown at 100 W in remote mode (Figure 8a,b), it can be seen that capacitance does not stabilize on a plateau, because of increased conductance in the same region. The leakage increasing in conductance with negative voltage (Figure 8b) is related to the effect of the rise of the capacitance in this region, being an order of magnitude smaller compared to the curves in Figure 8d,f, suggesting a reduction of the series resistance in the area of accumulation [67]. The sample with Al_2O_3 partial-monolayer grown at 100 W (Figure 8c,d) presented a high leakage current that decreased the accumulation capacitance. This higher leakage current in the accumulation region occurs due to a negative gate bias applied to the silicon *p*-type substrate. The majority carriers are attracted to the interface $Si/TiO_2/Al_2O_3$ with simultaneously accumulated minority carriers at the gate side flow through the TiO_2/Al_2O_3 layer, thus reducing the majority carriers' density at the interface

of $Si/TiO_2/Al_2O_3$. With the increase of gate bias, the accumulated majority carriers disappear, and a negative depletion region is formed in the silicon, which promotes a decrease of the leakage current and an increase of the capacitance, as shown by the peak in C-V curve (Figure 8c). In Figure 8e, an elongation in the C-V curve can be observed, which can be attributed to the existence of surface states in the TiO_2 thin films [68]. This behavior may be associated with increased ion damage due to the RF power at 150 W. For TiO_2 film growth at 150 W in remote mode, the C-V curve does not show any evidence of a decrease of the accumulation capacitance that allows to infer a drastic reduction of the leakage current. This reduction can be attributed to a structural rearrangement of the growth of the films at 150 W that reduced the series parasitic resistance (as shown in Table 1).

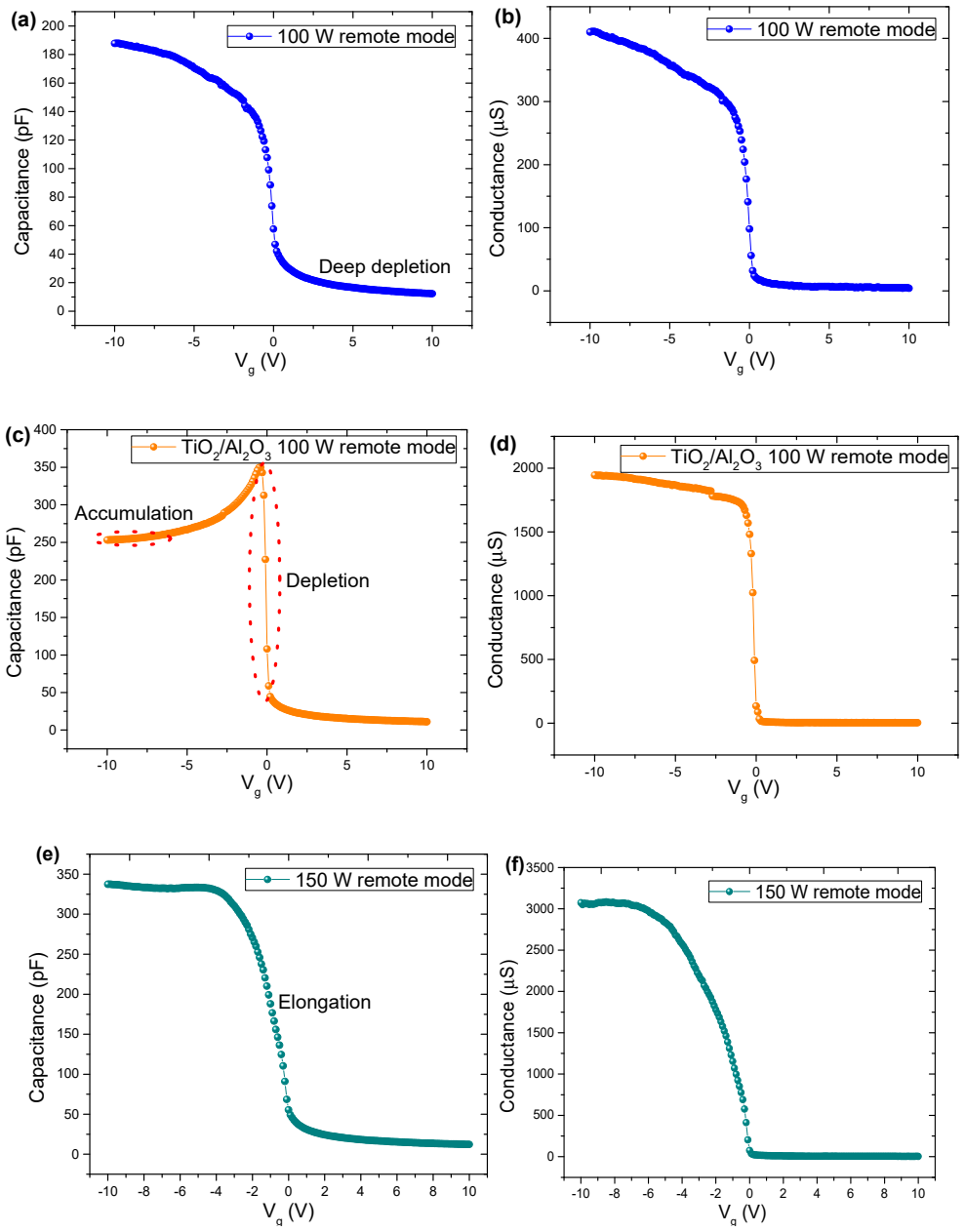

Figure 8. C-V and G-V curves for the fabricated MOS capacitors: (**a**) C-V curve for TiO_2 film grown in remote mode at 100 W, (**b**) G-V curve for TiO_2 film grown in remote mode at 100 W, (**c**) C-V curve for TiO_2 film grown in remote mode at 100 W, (**d**) G-V curve for TiO_2/Al_2O_3 film grown in remote mode at 100 W, (**e**) C-V curve for TiO_2 film grown in remote mode at 150 W and (**f**) G-V curve for TiO_2 film grown in remote mode at 150 W.

C-V and G-V curve characteristics for the samples deposited under direct exposure mode are shown in Figure 9. For capacitors with TiO_2 films grown at 150 W in direct mode, the C-V and G-V curves were only possible to be obtained in the range of −2 V to +2 V. The C-V curves (Figure 9a,c) showed a deep depletion region for both cases, as the behaviors for PEALD TiO_2/Si MOS capacitors with TiO_2 films grown in direct mode indicated a current leakage through the TiO_2 films. The sample with TiO_2 grown at 100 W in direct mode (Figure 9a) presented a low leakage current that raised the accumulation capacitance. This low leakage current in the accumulation region occurs due to an abrupt decreasing in conductance in the same negative bias region of the gate (Figure 9b). When the gate bias increase, the accumulation of the majority carriers disappears, and a negative depletion region is formed on the silicon, promoting a decrease in leakage current and an expansion of the capacitance, as shown by the peak in the C-V curve (Figure 9a).

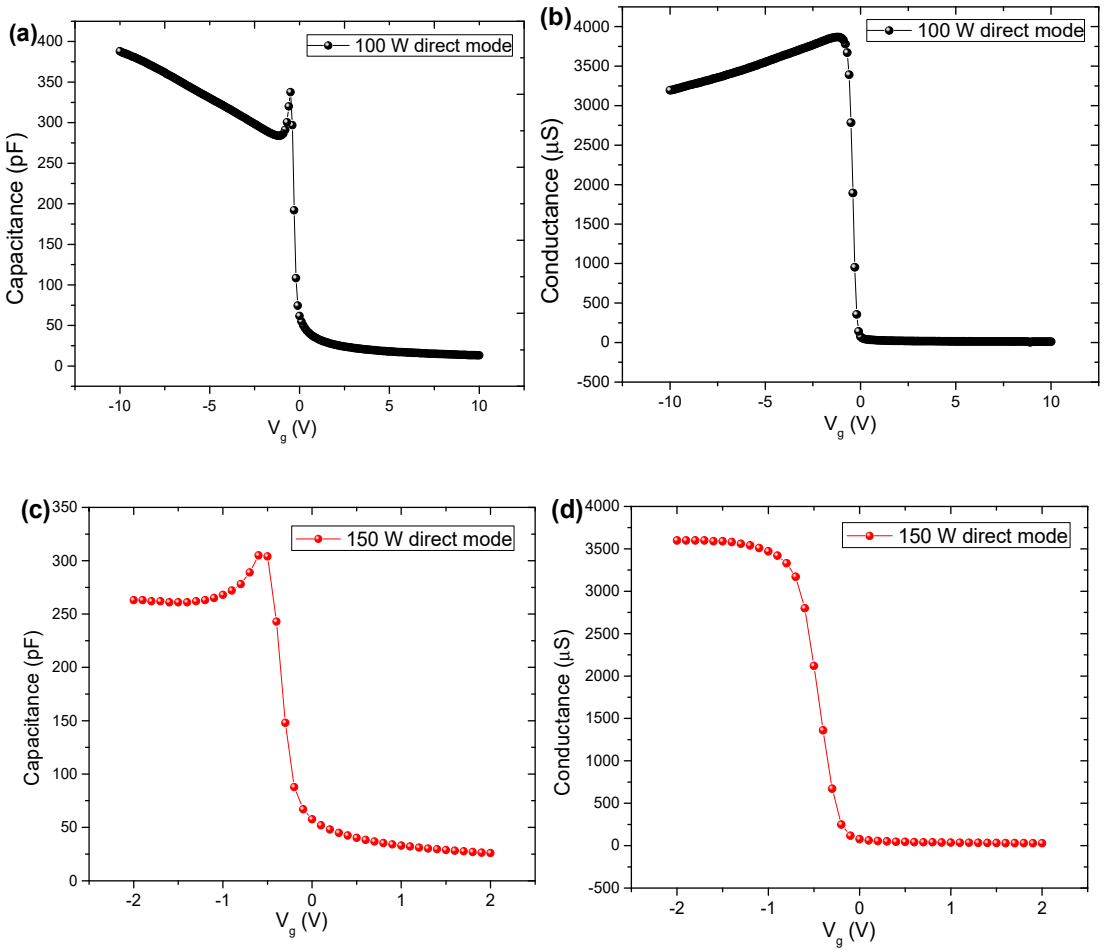

Figure 9. C-V and G-V curves for the fabricated MOS capacitors: (**a**) C-V curve for TiO_2 film grown in direct mode at 100 W, (**b**) G-V curve for TiO_2 film grown in direct mode at 100 W, (**c**) C-V curve for TiO_2 film grown in direct mode at 150 W and (**d**) G-V curve for TiO_2 film grown in direct mode at 150 W.

Compared to the 100 W TiO_2 thin film grown in remote mode, an increase in conductance by one order of magnitude occurs, probably due to the high ion bombardment caused by the direct exposure mode (Figure 9b). The insertion of Al_2O_3 partial-monolayers in TiO_2 film modulated the conductance (Figure 8d), with the maximum value of conductance at the ~2000 µS being between the values of TiO_2-100 W in remote mode (~400 µS) and TiO_2-100 W in direct mode (~4000 µS). It is noteworthy that for the sample grown at 150 W, in the direct mode, the same behavior in curves C-V and G-V was observed in relation to nanolaminate.

To better understand the electrical properties, we estimated another two parameters: (i) fixed insulator (TiO_2 and TiO_2/Al_2O_3) charges, Q_f; and (ii) the interface defects density, D_{it}, in the Si/insulator interface. We used Equation (7) to calculate Q_f, and to obtain the V_{fb}, we used the graphical method, which is shown in Figure 10 [66].

$$Q_f = \frac{C_{in}\left(\Phi_{ms} - V_{fb}\right)}{A.q} \tag{7}$$

where C_{in} is the capacitance of the insulator, A (4.3×10^{-3} cm^2) is the front metal contact area, q is the elementary charge, V_{fb} is the flat-band voltage, Φ_{ms} is the work function difference between the work function of metal (Al) and the work function of the semiconductor (Si) that was calculated from Equation (8) [69].

$$\Phi_{ms} = -0.6 - \frac{kT}{q}\ln\left(\frac{N_A}{n_i}\right), \tag{8}$$

where N_A is the doping concentration in the silicon ($N_A = 1.0 \times 10^{15}$ cm^{-3}), and n_i is the intrinsic concentration at room temperature ($n_i = 1.45 \times 10^{10}$ cm^{-3}) [68,70]. To use Equation (7), it was assumed, but not yet proved, that other charges have a reduced influence on Q_f measurements, and the interface traps are negligible [71–74]. The graphical method was used to find the Q_f values, taking into account the average of V_{fb} and C_{in}.

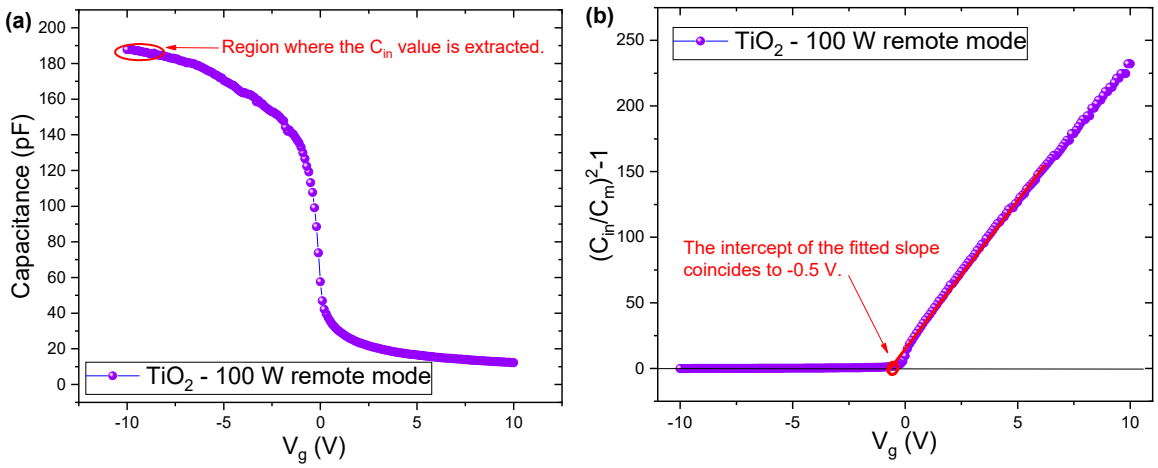

Figure 10. Nicollian and Brews [75] method used to calculate the capacitance of the insulator (C_{in}), flat-band voltage (V_{fb}) and fixed insulator charges (Q_f). (**a**) C-V curve showing the extract region of the C_{in} value, and (**b**) shows the typical V_{fb} extraction through the intercept of the fitted slope.

As can be seen in Figure 10a, the insulator capacitance value was extracted from the strong accumulation region in the C-V curve at negative bias due to the conductivity nature p-type of the silicon. To construct Figure 10b and extract the flat-band voltage, the following equation was used:

$$\left(\frac{C_{in}}{C_m}\right)^2 - 1 = 0, \tag{9}$$

where C_m is the experimentally measured capacitance. To calculate C_{in} and, consequently, Q_f, in the strong leakage processes from the capacitance lowering at the accumulation region of the C-V curves (Figures 7c and 8a,c), the Rajab Model was used [67]. To observe the leakage process, the Rajab model proposed a simplified electrical model, as shown in Figure 11a, where Y_C is an admittance which represents the leakage process, and R_S is the series resistance associated with the silicon substrate. $G_{m,max}$ and $C_{m,max}$ in Figure 11b are the accumulation conductance and capacitance, respectively, shown from a C-V meter.

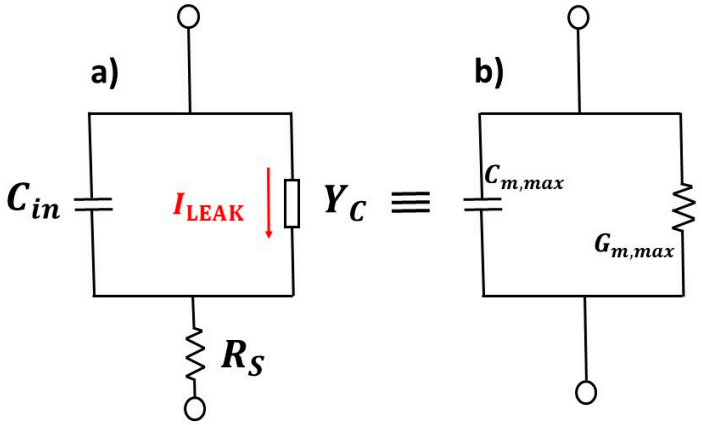

Figure 11. (**a**) Simplified electrical Rajab model. With Y_C being the admittance, which represents the leakage process, and R_S is the series resistance associated with the silicon substrate; and (**b**) measured $G_{m,max}$ and $C_{m,max}$, which are the accumulation conductance and capacitance, respectively.

Using the impedance equality of the electrical circuits shown in Figure 10a,b, we derived the equations for the leakage admittance Y_C and C_{in}, which are shown below [67]:

$$Y_C = \sqrt{\omega C_{in}\left(-\omega C_{in} + \omega C_{m,\,max}\left(1 + \frac{{G_{m,\,max}}^2}{(\omega C_{m,\,max})^2}\right)\right)}, \tag{10}$$

and

$$C_{in} = \frac{C_{m,\,max}\left((\omega C_{m,\,max})^2 + {G_{m,\,max}}^2\right)}{(\omega C_{m,\,max})^2 + \left(G_{m,\,max} - R_S\left((\omega C_{m,\,max})^2 + {G_{m,\,max}}^2\right)\right)}. \tag{11}$$

Table 2 shows the V_{fb} and Q_f values of all samples with the front contact area of 4.3×10^{-3} cm^2. As shown in the literature, TiO_2 grown on Si generates negative Q_f being more appropriate for rear passivation in solar cells, basically due to field-effect passivation [45]. Recently, Liao et al. [73] showed that TiO_x thin-film (63 nm) growth by ALD is also capable of providing passivation of c-Si substrates at the same level of thermal silicon oxide (SiO_2), silicon nitride (SiN_x) and aluminum oxide (Al_2O_3). This negative polarity corroborates with the best passivation performance in solar cells because negative Q_f repels minority carriers (electrons), resulting in an increased level of field-effect passivation [74].

Table 2. V_{fb} and Q_f calculated by using Nicollian and Brews method and the Rajab model.

Sample	V_{fb} (V)	Q_f (cm^{-2})
TiO_2-100 W remote mode	−0.5	-3.54×10^{11}
TiO_2/Al_2O_3-100 W remote mode	−0.4	-8.41×10^{11}
TiO_2-100 W direct mode	−0.2	-2.41×10^{12}
TiO_2-150 W direct mode	−0.4	-2.10×10^{12}
TiO_2-150 W remote mode	−0.3	-8.80×10^{11}

As can also be seen in Table 2, the exposure mode influences the values of the fixed charges but did not change the polarity. The increase in leakage in conductance with the negative voltage (Figure 7b) is related to the effect of the rise of the capacitance in this region of conductance that causes a reduced value in Q_f around 1×10^{11} cm^{-2} for the TiO_2-100 W in remote mode. The higher values were of the samples that grown in direct mode around 1×10^{12} cm^{-2} for both RF powers values. For the samples that grew at 100 W, a behavior similar to that of J-V curves was observed where the Al_2O_3 partial-monolayer modulated the values of the ideality factor. In this case, the Al_2O_3 partial-monolayer obtained a magnitude above the Q_f value obtained for TiO_2-100 W in remote mode and one order of

magnitude below the value obtained for the TiO_2-100 W in direct mode (as shown in Table 2), acting as a modulator between the two cases. As can be seen in Table 2, this analysis indicates that the fixed insulator charge values are not intrinsic to each insulator, and its concentration can be modified by exposure mode and plasma power.

Another critical parameter for the interface is the density of interface defects (D_{it}). For this, it was used the Hill–Coleman model [74], a single-frequency approximation for interface defects density determination, as shown below:

$$D_{it} = \frac{2}{A.q} \frac{\frac{G_{m,\ max}}{\omega}}{\left(\frac{G_{m,max}}{\omega.C_{in}}\right)^2 + \left(1 - \frac{C_{m,max}}{C_{in}}\right)^2}, \quad (12)$$

where $G_{m,max}$ is the maximum experimentally conductance, $C_{m,max}$ is the maximum experimentally capacitance and $\omega = 2\pi f$ (f = 1 MHz).

The advantage of this model is that only three measured values ($G_{m,max}$, $C_{m,max}$ and C_{in}) and a single frequency are needed. Therefore, the approximation is realized from the need of C-V and G-V plots. Table 3 summarizes the D_{it} values extracted with the help of Equation (12).

Table 3. Density of interface defects (D_{it}) calculated by Hill–Coleman model.

Sample	D_{it} ($eV^{-1}.cm^{-2}$)
TiO_2/Al_2O_3-100 W remote mode	5.52×10^{11}
TiO_2-100 W direct mode	7.08×10^{11}
TiO_2-100 W remote mode	2.44×10^{11}
TiO_2-150 W direct mode	3.48×10^{11}
TiO_2-150 W remote mode	6.74×10^{11}

Most of the samples show D_{it} values within the same order of magnitude, being the exception of the TiO_2-100 W in remote mode. This exception probably occurs due to the approximation technique for D_{it} is within 25–30% of the Nicollian–Brews peak D_{it}'s value between the flat band and mid-gap [71]. Since D_{it} is known to change by order of magnitude or more in the region between the flat band and mid-gap, this approximation is reasonable [74]. As suggested by Hill–Coleman, the frequency is into the MHz region. The results listed in Tables 2 and 3 show that the samples exhibit a density of interface defects (~10^{11}–10^{13} cm^{-2}) and a high density of negative fixed charges (~10^{11} $eV^{-1}.cm^{-2}$), which make them potential candidates for application in solar cells and DRAM technology. For example, TiO_2-100 W and TiO_2-150 W growth by the direct mode presents higher Q_f and lower D_{it}. These combined characteristics show the quality of these films to act as a passivation layer in solar cells. Cunha et al. [42] and Kotipali et al. [72] showed values in the same order of magnitude for Q_f (~10^{11}–10^{12} cm^{-2}) and D_{it} (~10^{10}–10^{12} eV^{-1} cm^{-2}) for other thin films, namely Al_2O_3, Si_3N_x and SiO_x. In both works, the films were grown on Si and CIGS.

To improve the discussion, we compared our results with works that used chemical and thermal treatments to enhance the electrical properties of the following structures Al_2O_3/Si and TiO_2/Al_2O_3/Si. Yoshitsugu et al. [76] deposited Al_2O_3 (25.2 nm) on Si by PEALD at a fixed temperature of the 100 °C and RF power at 400 W. They used high-pressure deuterium oxide annealing (HPDOA) treatment and reduced the leakage current density to an order of 10^{-7} A/cm^2. This result is two orders of magnitude lower than our results. Zougar et al. [77] deposited Al_2O_3 (~1 nm) on Si by the ultrasonic spray method. They used post-deposition annealing and post-metallization annealing as surface treatment. They showed values of for Q_f (~10^{10}–10^{11} cm^{-2}) and D_{it} (~10^{11}–10^{12} eV^{-1} cm^{-2}). Both results show a lower quality of these films in comparison with our films. Baek et al. [1] grew Al_2O_3 (50 nm), TiO_2 (50 nm) and Al_2O_3/TiO_2 (50 nm) on Si by PEALD at 100 °C and with RF power fixed at 200 W. They used several chemical treatments to modify the surface. The leakage current density values of Al_2O_3 and Al_2O_3/TiO_2 are, respectively, 10^{-8} and 10^{-9} A/cm^2. These values are lower than our results, but they

showed a leakage current density of the TiO_2 of the order of magnitude of 10^{-3} A/cm^2, which is two orders of magnitude higher than our values. Even without thermal or chemical treatment, our films have a high electrical quality, as shown in this brief comparison.

4. Conclusions

TiO_2 thin films were deposited on p-type Si substrates under different conditions by PEALD technique. Structural, chemical and morphological properties of the as-grown films were studied as a function of the following deposition parameters: RF power, substrate exposure mode and Al_2O_3 partial-monolayer insertion. Chemical composition determined by RBS analysis showed that the TiO_x films have an excess of oxygen content, with x values ranging from 2.13 ± 0.01 to 2.33 ± 0.01, which can be related to the higher reactivity of O_2 plasma. It was also observed that, with the insertion of Al_2O_3 partial-monolayers in TiO_2 to form the nanolaminate structure, an increase in the number of cycles to 2700 is necessary to obtain a film thickness close to pure TiO_2. GIXRD diffractograms showed a crystalline structure for all pure TiO_2 thin films with a crystalline degree of 87.1% to 95.9%. The Al_2O_3 partial-monolayer reduced TiO_2 crystallinity degree to 34.2%. Raman spectra allow us to observe that the shift in the signal peak at 144 cm^{-1} and its bandwidth is related to the increase of oxygen content in PEALD TiO_2 films. FESEM study evidenced the effect of the electrode grid on the reduction of the action of the plasma ions during the capacitively coupled PEALD process. It can be seen, for both power values investigated, that the change from remote to direct mode caused a slight reduction in grain size, probably due to the more significant action of species impinging from plasma to substrate. The insertion of Al_2O_3 partial-monolayers into TiO_2 film disrupts the growth of crystalline grains, creating only a few nanocrystalline grains in the amorphous matrix. PEALD TiO_2/p-type Si MOS capacitors were fabricated by depositing of Al electrical contacts. J-V, C-V and G-V measurements of these capacitors were performed. The Ortiz-Conde model was used to fit the experimental dark J-V curves and values between 1.59 to 1.99 were obtained for the ideality factor. For TiO_2 thin-film growth at RF power of 150 W, the values did not change with the exposure mode, and this behavior suggests that the power effect is predominant in the process. For the sample TiO_2-100 W, different values of the ideality factor were found: 1.93 (direct mode) and 1.79 (remote mode). For the TiO_2/Al_2O_3 nanolaminate, the ideality factor was 1.59, suggesting that the insertion of Al_2O_3 partial-monolayers can tune the ideality factor. C-V and G-V curves showed a deep depletion region for all cases, which indicates the absence of a layer of inversion because of the high leakage of electrons through the TiO_2 films. It was noted that Al_2O_3 partial-monolayer, grown at 100 W, modulated the conductance with the maximum value of ~2000 μS, whereas a value of ~400 μS and ~4000 μS were found for TiO_2-100 W in remote mode and TiO_2-100 W in direct mode, respectively. The fixed insulator charges (Q_f) and the interface defects density (D_{it}) were also estimated. In summary, the fabricated PEALD TiO_2/p-type Si MOS capacitors exhibit electrical characteristics suitable for microelectronics and photovoltaics applications.

Author Contributions: All authors have read and agree to the published version of the manuscript. Conceptualization, W.C. and S.d.S.F.; methodology, W.C. and R.P.; formal analysis, W.C., V.D., G.T., R.P., M.W. and R.R.; investigation, W.C., V.D., M.F., G.T., R.P. and M.W.; resources: H.M., S.d.S.F. and R.P.; writing—original draft, W.C.; writing—review and editing, W.C., R.P., M.F., H.M. and S.d.S.F.; supervision, S.d.S.F. and R.P.; funding acquisition, H.M., S.d.S.F., R.P. and M.F. All authors have read and agreed to the published version of the manuscript.

Funding: The financial support of the Brazilian agency program FAPESP/MCT/CNPq-PRONEX (grant no. 2011/50773-0), FAPESP (grant no. 2015/05956-0, no. 2015/10876-6, no. 2016/17826-7, and no. 2018/01265-1), CNPq (grant no. 305496/2012-3, 446545/2014-7 and 437921/2018-2), CAPES (grant no. 23038.005802/2014-98) and the Brazilian Space Agency (AEB/Uniespaço) is also gratefully acknowledged.

Acknowledgments: The authors are grateful to T.F. da Silva from the Physics Department—USP for the RBS measurements and I.Y. Abe from LME-USP for the Raman spectroscopy measurements.

Conflicts of Interest: The authors declare no conflicts of interest.

References

1. Baek, Y.; Lim, S.; Kim, L.H.; Park, S.; Lee, S.W.; Oh, T.H.; Kim, S.H.; Park, C.E. Al_2O_3/TiO_2 nanolaminate gate dielectric films with enhanced electrical performances for organic field-effect transistors. *Org. Electron.* **2016**, *28*, 139–146. [CrossRef]
2. Wei, D.; Edgar, J.H.; Briggs, D.P.; Retterer, S.T.; Srijanto, B.; Hensley, D.K.; Meyer, H.M., III. Atomic layer deposition TiO_2-Al_2O_3 stack: An improved gate dielectric on Ga-polar GaN metal oxide semiconductor capacitors. *J. Vac. Sci. Technol. B* **2014**, *32*, 060602. [CrossRef]
3. Jeong, H.Y.; Kim, Y.I.; Lee, J.Y.; Choi, S.-Y. A low-temperature-grown TiO_2-based device for the flexible stacked RRAM application. *Nanotechnology* **2010**, *21*, 115203. [CrossRef] [PubMed]
4. Zhang, W.; Kong, J.-Z.; Cao, Z.-Y.; Li, A.-D.; Wang, L.-G.; Zhu, L.; Li, X.; Cao, Y.-Q.; Wu, D. Bipolar resistive switching characteristics of $HfO_2/TiO_2/HfO_2$ trilayer-structure RRAM devices on Pt and TiN-coated substrates fabricated by atomic layer deposition. *Nanoscale Res. Lett.* **2017**, *12*, 393. [CrossRef] [PubMed]
5. Wei, D.; Hossain, T.; Garces, N.Y.; Nepal, N.; Meyer, H.M., III; Kirkham, M.J.; Eddy, C.R., Jr.; Edgar, J.H. Influence of atomic layer deposition temperatures on TiO_2/n-Si MOS capacitor. *ECS J. Solid State Sci. Technol.* **2013**, *2*, N110–N114. [CrossRef]
6. Maeng, W.J.; Kim, W.-H.; Lim, S.J.; Lee, C.-S.; Lee, T.; Kim, H. Flatband voltage control in p-metal gate metal-oxide-semiconductor field effect transistor by insertion of TiO_2 layer. *Appl. Phys. Lett.* **2010**, *96*, 082905. [CrossRef]
7. Zardetto, V.; Williams, B.L.; Perrota, A.; Di Giacomo, F.; Verheijen, M.A.; Andriessen, R.; Kessels, W.M.M.; Creatore, M. Atomic layer deposition for perovskite solar cells: Research status, opportunities, and challenges. *Sustain. Energy Fuels* **2017**, *1*, 30–55. [CrossRef]
8. Wang, W.-C.; Tsai, M.-C.; Yang, J.; Hsu, C.; Chen, M.-J. Efficiency enhancement of nanotextured black silicon solar cells using Al_2O_3/TiO_2 dual-layer passivation stack prepared by atomic layer deposition. *ACS Appl. Mater. Interfaces* **2015**, *7*, 10228–10237. [CrossRef]
9. Pessoa, R.S.; Fraga, M.A.; Santos, L.V.; Massi, M.; Maciel, H.S. Nanostructured thin films based on TiO_2 and/or SiC for use in photoelectrochemical cells: A review of the material characteristics, synthesis and recent applications. *Mater. Sci. Semicond. Process.* **2015**, *29*, 56–68. [CrossRef]
10. Nakata, K.; Fujishima, A. TiO_2 photocatalysis: Desing and applications. *J. Photochem. Photobiol. C* **2012**, *13*, 169–189. [CrossRef]
11. Daghrir, R.; Drogui, P.; Robert, D. Modified TiO_2 for environmental photocatalytic applications: A review. *Ind. Eng. Chem. Res.* **2013**, *52*, 3581–3599. [CrossRef]
12. Pessoa, R.S.; Fraga, M.A.; Chiappim, W.; Maciel, H.S. Exploring the Properties and Fuel Cell Applications of Ultrathin Atomic Layer Deposited Metal Oxide Films. In *Emerging Materials for Energy Conversion and Storage*, 1st ed.; Cheong, K.Y., Impellizzeri, G., Fraga, M.A., Eds.; Elsevier: Cambridge, MA, USA, 2018; pp. 83–114.
13. Sharma, R.K.; Bhatnagar, M.C.; Sharma, G.L. Influence of doping on sensitivity and response time of TiO_2 oxygen gas sensor. *Rev. Sci. Instrum.* **1999**, *71*, 1500–1509. [CrossRef]
14. Bao, S.-J.; Li, C.M.; Zang, J.-F.; Cui, X.-Q.; Qiao, Y.; Guo, J. New nanostructured TiO_2 for Direct electrochemistry and glucose sensor applications. *Adv. Funct. Mater.* **2008**, *18*, 591–599. [CrossRef]
15. Fraga, M.A.; Furlan, H.; Pessoa, R.S.; Rasia, L.A.; Mateus, C.F.R. Studies on SiC, DLC and TiO_2 thin films as piezoresistive sensor materials for high-temperature applications. *Microsyst. Technol.* **2012**, *8*, 1027–1033. [CrossRef]
16. Rathee, D.; Kumar, M.; Arya, S.K. CMOS development and optimization, scaling issue and replacement with high-k material for future microelectronics. *Int. J. Comput. Appl.* **2010**, *8*, 10–17. [CrossRef]
17. Pfeiffer, K.; Schulz, U.; Tünnermann, A.; Szeghalmi, A. Antireflection coating for strongly curved glass lenses by atomic layer deposition. *Coatings* **2017**, *7*, 118. [CrossRef]
18. Pessoa, R.S.; Fraga, M.A. Biomedical applications of ultrathin atomic layer deposited metal oxide films on polymeric materials. In *Frontiers of Nanoscience*, 1st ed.; Benelmekki, M., Erbe, A., Eds.; Elsevier: Cambridge, MA, USA, 2019; Volume 14, pp. 291–307.
19. Pessoa, R.S.; dos Santos, V.P.; Cardoso, S.B.; Doria, A.C.O.C.; Figueira, F.R.; Rodrigues, B.V.M.; Testoni, G.E.; Fraga, M.A.; Marciano, F.R.; Lobo, A.O.; et al. TiO_2 coatings via atomic layer deposition on polyurethane and polydimethylsiloxane substrate: Properties and effects on *C. Albicans* growth and inactivation process. *Appl. Surf. Sci.* **2017**, *422*, 73–84. [CrossRef]

20. Dias, V.; Maciel, H.S.; Fraga, M.A.; Lobo, A.O.; Pessoa, R.S.; Marciano, F.R. Atomic layer deposited TiO_2 and Al_2O_3 thin films as a coating for Aluminum food packing application. *Materials* **2019**, *12*, 682. [CrossRef]
21. Uchiyama, H.; Bando, T.; Kozuka, H. Effect of the amount of H_2O and HNO_3 in $Ti(OC_3H_7^i)_4$ solutions on the crystallization of sol-gel-derived TiO_2 films. *Thin Solid Film.* **2019**, *669*, 157–161. [CrossRef]
22. Abbas, F.; Bensaha, R.; Taroré, H. The influence of Zn^{+2} doping and annealing temperature on grown-up of nanostructures TiO_2 thin films prepared by the sol-gel dip-coating method and their photocatalytic application. *Optik* **2019**, *180*, 361–369. [CrossRef]
23. Toku, H.; Pessoa, R.S.; Maciel, H.S.; Massi, M.; Mengui, U.A. The effect of oxygen concentration on the low temperature deposition of TiO_2 thin films. *Surf. Coat. Technol.* **2008**, *202*, 2126–2131. [CrossRef]
24. Toku, H.; Pessoa, R.S.; Maciel, H.S.; Massi, M.; Mengui, U.A. Influence of process parameters on the growth of pure-phase anatase and rutile TiO_2 thin films deposited by low temperature reactive magnetron sputtering. *Braz. J. Phys.* **2010**, *40*, 340–343. [CrossRef]
25. Astinchap, B.; Laelabadi, K.G. Effects of substrate temperature and precursor amount on optical properties and microstructure of CVD deposited amorphous TiO_2 thin films. *J. Phys. Chem. Solids* **2019**, *129*, 217–226. [CrossRef]
26. Manova, D.; Arias, L.F.; Holefe, A.; Alani, I.; Kleiman, A.; Asenova, I.; Decker, U.; Marquez, A.; Mändl, S. Nitrogen incorporation during PVD deposition of TiO_2: N thin films. *Surf. Coat. Technol.* **2017**, *312*, 61–65. [CrossRef]
27. Pessoa, R.S.; Pereira, F.P.; Testoni, G.E.; Chiappim, W.; Maciel, H.S.; Santos, L.V. Effect of substrate type on the structure of TiO_2 thin films deposited by atomic layer deposition technique. *JICS* **2015**, *1*, 38–42.
28. Chiappim, W.; Testoni, G.E.; Moraes, R.S.; Sagás, J.C.; Origo, F.D.; Vieira, L.; Maciel, H.S. Structural, morphological, and optical properties of TiO_2 thin films grown by atomic layer deposition on fluorine-doped tin oxide conductive glass. *Vacuum* **2016**, *123*, 91–102. [CrossRef]
29. Lim, J.W.; Yuu, S.J.; Lee, J.H. Characteristics of TiO_2 films prepared by ALD with and without plasma. *Electrochem. Solid State Lett.* **2004**, *11*, F73–F76. [CrossRef]
30. Lee, J.; Lee, S.J.; Han, W.B.; Jeon, H.; Park, J.; Jang, W.; Yoon, C.S.; Jeon, H. Deposition temperature dependence of titanium oxide thin films grown by remote-plasma atomic layer deposition. *Phys. Status Solidi A* **2013**, *210*, 276–284. [CrossRef]
31. Kilpi, L.; Ylivaara, O.M.E.; Vaajoki, A.; Liu, X.; Rontu, V. Tribological properties of thin films made by atomic layer deposition sliding against silicone. *J. Vac. Sci. Technol. A* **2018**, *36*, 01A122. [CrossRef]
32. Faraz, T.; Knoops, H.C.M.; Verheijen, M.A.; van Helvoirt, C.A.A.; Karwal, S.; Sharma, A.; Beladiya, V.; Szeghalmi, A.; Hausmann, D.M.; Henri, J.; et al. Tuning material properties of oxides and nitrides by substrates biasing during plasma-enhanced atomic layer deposition on planar and 3D substrate topographies. *ACS Appl. Mater. Interfaces* **2018**, *10*, 13158–13180. [CrossRef]
33. Chaker, A.; Szkutnik, P.D.; Pointet, J.; Gonon, P.; Vallée, C.; Bsiesy, A. Understanding the mechanisms of interfacial reaction during TiO_2 layer growth on RuO_2 by atomic layer deposition with O_2 plasma or H_2O as oxygen source. *J. Appl. Phys.* **2016**, *120*, 085315. [CrossRef]
34. Choi, W.-S. X-ray photoelectron spectroscopy analyses of atomic layer deposition-prepared titanium-dioxide thin films with oxygen sources and their annealing effect. *Sci. Adv. Mater.* **2016**, *8*, 336–341. [CrossRef]
35. Ratzsch, S.; Kley, E.-B.; Tünnermann, A.; Szeghalmi, A. Influence of the oxygen plasma parameters on the atomic layer deposition of titanium dioxide. *Nanotechnology* **2015**, *26*, 024003. [CrossRef] [PubMed]
36. Schindler, P.; Logar, M.; Provine, J.; Prinz, F.B. Enhanced step coverage of TiO_2 deposited on high aspect ratio surfaces by plasma-enhanced atomic layer deposition. *Langmuir* **2015**, *31*, 5057–5062. [CrossRef]
37. Puurunen, R.L. Surface chemistry of atomic layer deposition: A case study for the trimethylaluminum/water process. *J. Appl. Phys.* **2005**, *97*, 121301. [CrossRef]
38. Profijt, H.B.; Potts, S.E.; van de Sanden, M.C.M.; Kessels, W.M.M. Plasma-assisted atomic layer deposition: Basics, opportunities, and challenges. *J. Vac. Sci. Technol. A* **2011**, *29*, 050801. [CrossRef]
39. Potts, S.E.; Kessels, W.M.M. Energy-enhanced atomic layer deposition for more process and precursor versatility. *Coord. Chem. Rev.* **2013**, *257*, 3254–3270. [CrossRef]
40. Liu, G.X.; Shan, F.K.; Park, J.J.; Lee, W.J.; Lee, G.H.; Kim, I.S.; Shin, B.C.; Yoon, S.G. Electrical properties of Ga_2O_3-based dielectric thin films prepared by plasma enhanced atomic layer deposition (PEALD). *J. Electroceram.* **2006**, *17*, 145–149. [CrossRef]

41. Hudec, B.; Huseková, K.; Aarik, J.; Tarre, A.; Kasikov, A.; Frölich, K. RuO2/TiO2 based MIM capacitors for DRAM applications. In Proceedings of the 8th International Conference on Advanced Semiconductor Devices and Microsystems, Smolenice Castle, Slovakia, 25–27 October 2010; pp. 341–344.
42. Cunha, J.M.V.; Fernandes, P.A.; Hultqvist, A.; Teixeira, J.P.; Bose, S.; Vermang, B.; Garud, S.; Buldu, S.; Gaspar, J.; Edoff, Leitão, J.P.; et al. Insulator Materials for Interface Passivation of Cu(In, Ga)Se_2 thin films. *IEEE J. Photovolt.* **2018**, *8*, 1313–1319. [CrossRef]
43. Kim, H.; Oh, I.-K. Review of plasma-enhanced atomic layer deposition: Technical enabler of nanoscale device fabrication. *Jpn. J. Appl. Phys.* **2014**, *53*, 03DA01. [CrossRef]
44. Choi, G.-J.; Kim, S.K.; Won, S.-J.; Kim, H.J.; Hwang, C.S. Plasma-enhanced atomic layer deposition of TiO_2 and Al-doped TiO_2 films using N_2O and O_2 reactants. *J. Electrochem. Soc.* **2009**, *156*, G138–G143. [CrossRef]
45. Chiappim, W.; Testoni, G.E.; Doria, A.C.O.C.; Pessoa, R.S.; Fraga, M.A.; Galvão, N.K.A.M.; Grigorov, K.G.; Vieira, L.; Maciel, H.S. Relationships among growth mechanism, structure and morphology of PEALD TiO_2 films: The influence of O_2 plasma power, precursors chemistry and plasma exposure mode. *Nanotechnology* **2016**, *27*, 305701. [CrossRef] [PubMed]
46. Kääriäinen, T.O.; Cameron, D.C. Plasma-enhanced atomic layer deposition of Al_2O_3 at room temperature. *Plasma Process. Polym.* **2009**, *6*, S237–S241. [CrossRef]
47. Nogueira, W.A.; dos Santos Filho, S.G. Influência das limpezas químicas úmidas $H_2O/H_2O_2/NH_4OH$ e $H_2O/HF/HNO_3$ na micro-rugosidade de lâminas de silício. *Revista Brasileira de Aplicações de Vácuo* **2001**, *20*, 46–51.
48. Faraz, T.; Arts, K.; Karwal, S.; Knoops, H.C.M.; Kessels, W.M.M. Energetic ions during plasma-enhenced atomic layer deposition and their role in tailoring materials properties. *Plasma Sources Sci. Technol.* **2019**, *28*, 024002. [CrossRef]
49. Testoni, G.E.; Chiappim, W.; Pessoa, R.S.; Fraga, M.A.; Miyakawa, W.; Sakane, K.K.; Galvão, N.K.A.M.; Vieira, L.; Maciel, H.S. Influence of the Al_2O_3 partial-monolayer number on the crystallization mechanism of TiO_2 in ALD TiO_2/Al_2O_3 nanolaminates and its impact on the material properties. *J. Phys. D Appl. Phys.* **2016**, *49*, 375301. [CrossRef]
50. LAMFI. Available online: http://deuterio.if.usp.br/multisimnra/ (accessed on 3 December 2019).
51. MPCDF. Available online: https://home.mpcdf.mpg.de/~{}mam/Mayer-AIP-Conference-Proceedings-475- (accessed on 20 December 2019).
52. Chiappim, W.; Testoni, G.E.; de Lima, J.S.B.; Medeiros, H.S.; Pessoa, R.S.; Grigorov, K.G.; Vieira, L.; Maciel, H.S. Effect of process temperature and reaction cycle number on atomic layer deposition of TiO_2 thin films using $TiCl_4$ and H_2O precursors: Correlation between material properties and process environment. *Braz. J. Phys.* **2016**, *46*, 56–69. [CrossRef]
53. Bousoulas, P.; Michelakaki, I.; Tsoukalas, D. Influence of oxygen content of room temperature TiO_{2-x} deposited films for enhanced resistive switching memory performance. *J. Appl. Phys.* **2014**, *115*, 034516. [CrossRef]
54. Ohsaka, T.; Izumi, F.; Fujiki, Y. Raman spectrum of anatase, TiO_2. *J. Raman Spectrosc.* **1978**, *7*, 321–324. [CrossRef]
55. Parker, J.C.; Siegel, R.W. Calibration of the Raman spectrum to the oxygen stoichiometry of nanophase TiO_2. *Appl. Phys. Lett.* **1990**, *57*, 943. [CrossRef]
56. Bassi, A.L.; Cattaneo, D.; Russo, V.; Bottani, C.E.; Barborini, E.; Mazza, T.; Piseri, P.; Miliani, P.; Ernst, F.O.; Wegner, K.; et al. Raman spectroscopy characterization of titania nanoparticles produced by flame pyrolysis: The influence of size and stoichiometry. *J. Appl. Phys.* **2005**, *98*, 074305. [CrossRef]
57. Gates-Rector, S.; Blanton, T. The powder diffraction file: A quality materials characterization database. *Powder Diffr.* **2019**, *34*, 352–360. [CrossRef]
58. Avila, J.R.; Qadri, S.B.; Freitas, J.A., Jr.; Nepal, N.; Boris, D.R.; Walton, S.G.; Eddy, C.R., Jr.; Wheeler, V.D. Impact of growth conditions on the phase selectivity and epitaxial quality of TiO_2 films grown by plasma-assisted atomic layer deposition. *Chem. Mater.* **2019**, *31*, 3900–3908. [CrossRef]
59. Patterson, A.L. The Scherrer formula for X-ray particle size determination. *Phys. Rev.* **1939**, *56*, 978. [CrossRef]
60. Ortiz-Conde, A.; Sánchez, F.J.G.; Muci, J. New method to extract the model parameters of solar cells from the explicit analytic solutions of their illuminated I–V characteristics. *Sol. Energy Mater. Sol. Cells* **2006**, *90*, 352–361. [CrossRef]

61. Corless, R.M.; Gonnet, G.H.; Hare, D.E.G.; Jeffrey, D.J.; Knuth, D.E. On the Lambert W Function. *Adv. Comput. Math.* **1996**, *5*, 329–359. [CrossRef]
62. Shockley, W. The theory of p-n junctions in semiconductors and p-n junction transistors. *Bell Syst. Tech. J.* **1949**, *28*, 435–489. [CrossRef]
63. Sah, C.; Noyce, R.N.; Shockley, W. Carrier generation and recombination in p-n junctions and p-n junction characteristics. *Proc. IRE* **1957**, *45*, 1228–1243. [CrossRef]
64. Faulkner, E.A.; Buckingham, M.J. Modified theory of the current/voltage relation in silicon p-n junctions. *Electron. Lett.* **1968**, *4*, 359–360. [CrossRef]
65. Nussbaum, A. Generation-recombination characteristic behavior of silicon diodes. *Phys. Status Solidi A* **1973**, *19*, 441–450. [CrossRef]
66. Jain, A.; Kapoor, A. A new method to determine the diode ideality factor of real solar cell using Lambert W-function. *Sol. Energy Mater. Sol. Cells* **2005**, *85*, 391–396. [CrossRef]
67. Rajab, S.M.; Oliveira, I.C.; Massi, M.; Maciel, H.S.; dos Santos Filho, S.G.; Mansano, R.D. Effect of the thermal annealing on the electrical and physical properties of SiC thin films produced by RF magnetron sputtering. *Thin Solid Film.* **2006**, *512*, 170–175. [CrossRef]
68. Oliveira, I.C.; Massi, M.; Santos, S.G.; Otani, C.; Maciel, H.S.; Mansano, R.D. Dieletric characteristics of AlN films grown by d.c.-magnetron sputtering discharge. *Diam. Relat. Mater.* **2001**, *10*, 1317–1321. [CrossRef]
69. Schroder, D.K. *Semiconductor Material and Device Characterization*, 3rd ed.; Wiley: Hoboken, NJ, USA, 2005.
70. Dingemans, G.; Terlinden, N.M.; Verheijen, M.A.; van de Sanden, M.C.M.; Kessels, W.M.M. Controlling the fixed charge and passivation of Si (100)/Al_2O_3 interfaces using ultrathin SiO_2 interlayers synthesized by atomic layer deposition. *J. Appl. Phys.* **2011**, *110*, 093715. [CrossRef]
71. Tang, X.; Francis, L.A.; Simonis, P.; Haslinger, M.; Delamare, R.; Deschaume, O.; Flandre, D.; Defrance, P.; Jonas, A.M.; Vigneron, J.P.; et al. Room temperature atomic layer deposition of Al_2O_3 and replication of butterfly wings for photovoltaic application. *J. Vac. Sci. Technol. A* **2011**, *30*, 01A146. [CrossRef]
72. Kotipali, R.; Delemare, R.; Poncelet, O.; Tang, X.; Francis, L.A.; Flandre, D. Passivation effects of atomic-layer-deposited aluminum oxide. *EPJ Photovolt.* **2013**, *4*, 1–8. [CrossRef]
73. Liao, B.; Hoex, B.; Arbele, A.G.; Chi, D.; Bhatia, C.S. Excellent c-Si surface passivation by low-temperature atomic layer deposited titanium oxide. *Appl. Phys. Lett.* **2014**, *104*, 253903. [CrossRef]
74. Hill, W.A.; Coleman, C.C. A single-frequency approximation for interface-state density determination. *Solid State Electron.* **1979**, *23*, 987–993. [CrossRef]
75. Nicollian, E.H.; Brews, J.R. MOS (metal oxide semiconductor) physics and technology. *J. Vac. Sci. Technol.* **1982**, *21*, 1048.
76. Yoshitsugu, K.; Horita, M.; Ishikawa, Y.; Uraoka, Y. Leakage current reduction in ALD-Al_2O_3 dieletric deposited on Si by pressure deuterium oxide annealing. *ECS Trans.* **2015**, *67*, 205–210. [CrossRef]
77. Zougar, L.; Sali, S.; Kermadi, S.; Boucheham, A.; Boumaour, M.; Kechouane, M. Annealling impact on interface properties of sprayed Al_2O_3-based MIS structure for silicon surface passivation. *J. Electron. Mater.* **2019**, *48*, 916–924. [CrossRef]